Extension of roughness noise to bluff bodies using the boundary element method

Antoni Alomar*, David Angland*

Faculty of Engineering and the Environment, University of Southampton, Southampton, Hampshire, SO16 7QF, UK

Xin Zhang

Department of Mechanical and Aerospace Engineering, The Hong Kong University of Science and Technology, Clear Water Bar, Kowloon, Hong Kong SAR, China

Abstract

A prediction model of roughness noise generated by bluff body flow at high Reynolds numbers is proposed. Howe's roughness noise theory extended by Liu and Dowling is used, and the boundary layer inputs to the theory have been modified for a bluff body. The scattering due to the bluff body has been accounted for by the boundary element method. The procedure to couple the roughness noise sources to the tailored Green's function is detailed for the case where the boundary element method mesh is orthogonal and aligned with the boundary layer outer velocity. The proposed method has been implemented and compared to experimental results for the particular case of a circular cylinder with large roughness. Two different estimations of the skin friction, which is an input to the roughness noise theory, are considered. One is a zero-pressure gradient model, and the second is based on published experimental data of the skin friction on a rough circular cylinder, but with smaller roughness than was used in the experiments. The zero-pressure gradient skin friction estimate leads to a better prediction of the effect of changes in the area covered by roughness elements. The success of the zero-pressure gradient skin friction estimate is

*Corresponding author

Email addresses: tonignasi@gmail.com (Antoni Alomar), d.angland@soton.ac.uk (David Angland), aexzhang@ust.hk (Xin Zhang)

encouraging as the only modifications that need to be made to the boundary layer model to account for a bluff body are the boundary layer outer velocity distribution and the location of separation.

Keywords: Roughness noise, boundary element method, bluff body, aeroacoustics

1. Introduction

There is a growing global effort to reduce noise pollution due to aircraft. The aeroacoustics of aircraft has been the subject of intense research over several decades. New aircraft must meet certification levels for noise. Therefore, noise prediction tools are increasingly important in the design phase.

Most aircraft contain surface irregularities in the form of small components laying on the surface, e.g. protrusions, joints, ridges, etc. These small components contribute significantly to the high frequency noise. The first prediction schemes for landing gear noise did not consider the small components, which resulted in Equivalent Perceived Noise Level underprediction of up to 8 dB [1]. It was postulated that the underprediction was due to an inadequate description of high-frequency noise, as well as neglecting the small components. Subsequent prediction models included more accurate descriptions of the high frequency noise, such as the statistical model of Guo [2]. In this model, the far field spectrum was derived in terms of the surface pressure spectrum assuming uncorrelated noise sources. A later model by the same author [3] accounted explicitly for the small elements, but through empirical laws with limited predictive power.

A simplified view of the effect of small components or roughness elements on noise generation is as follows. On the upstream face of a component, a boundary layer grows until separation, and the small components on the surface are immersed in it. The noise generated through the interaction of the turbulent field with the surface elements is described by roughness noise theory. For this description to be valid, it is required that the bluff body surface is approxi-

mately flat over distances of the order of the roughness size, and that the small components are fully immersed in a turbulent boundary layer.

The main advantage of this approach is that roughness noise theory provides a physical description of the noise generation mechanism. Also, the approach should be better at higher Reynolds numbers, where transition occurs further upstream and more small components will be immersed in a fully developed turbulent boundary layer. The main weakness is the simplification of real geometries to generic distributed roughness elements. It is clear that the resulting model will be at most an approximation. However, it will potentially have greater predictive power than a purely empirical approach.

A previous experimental study [4] showed that roughness noise was dominant over a wide frequency range for both a flat plate and a circular cylinder with large distributed roughness (by large roughness it is meant, not only that the turbulent boundary layer is in the fully rough regime, but also that the roughness height is comparable to the boundary layer thickness). The discrepancies between the experiments and Howe's theory were mostly attributed to roughness edge effects. It was argued that two main issues need to be addressed in order to apply roughness noise theory to bluff bodies. Firstly, the rough wall boundary layer model must be adapted for a bluff body. Secondly, the scattering of roughness noise by the bluff body needs to be accounted for.

For the sake of generality, the boundary element method (BEM) has been used to account for the scattering on the bluff body. For the two-dimensional case as well as the three-dimensional axisymmetric case, analytical solutions exist [5, 6]. However, the proposed prediction model is capable of dealing with arbitrary bluff body shapes and represents a general approach. In addition, a novel procedure to couple the BEM solution to the roughness noise sources has been proposed, based on combining the surface monopoles into surface dipoles to model the roughness noise sources.

The proposed model has been implemented and compared against experimental results for the case of a circular cylinder. The reason is twofold. Firstly, it is a representative geometry of landing gear components, and secondly, there

is more experimental and computational data in the literature than for other bluff bodies. The calculation of the boundary layer evolution and the determination of the roughness noise dipole sources are particularly simple in this case, where the natural surface mesh is orthogonal and aligned with the boundary layer outer velocity. However, the methodology proposed is applicable to arbitrary bluff body geometries.

The structure of the paper is as follows. Firstly, the literature on roughness noise and on rough wall boundary layers subject to a favourable pressure gradient are revised. Secondly, the rough wall boundary layer model for the case of a circular cylinder is detailed. Thirdly, the validation of BEM applied to a three-dimensional circular cylinder is presented. The coupling of the roughness noise model with the tailored Green's function obtained from BEM is also presented. Lastly, the outputs from the resulting prediction model are compared to experimental data, and a parametric study of the far field noise dependence on roughness size and surface density is presented.

2. Background

2.1. Roughness noise

Roughness noise constitutes an important source of sound in many engineering applications. Owing to the high Reynolds number nature of the problem, it has mainly been studied experimentally [4, 7, 8, 9, 10, 11]. The roughness elements act as compact dipole sources with streamwise and spanwise components. Several numerical studies have also been performed [12, 13], focusing on the flow features in the vicinity of the roughness elements and their relationship to the far field noise.

Based on experimental evidence and the theory of rough wall boundary layers, several theoretical approaches have been developed [14, 15, 16]. Howe's approach [14] assumes that roughness consists of hemispherical bosses, which scatter the quadrupole noise sources within the boundary layer. It is assumed that quadrupole noise sources contained within the interstitial flow are negligi-

ble compared to the ones above the roughness elements. This approximation, together with Townsend's similarity hypothesis [17, 18, 19, 20], implies that a smooth wall pressure spectrum, appropriately scaled to account for roughness, can be used. Liu and Dowling [21] extended the theory of Howe, substituting the asymptotic approximation of the integral over wavenumber space, with an exact numerical integration. Liu *et al.* [9] determined the streamwise and spanwise dipole strengths of a single roughness element, for given properties of the boundary layer. Liu and Dowling's scheme has been shown to accurately predict the roughness noise peak level and frequency for large hemispherical roughness [4]. The theoretical approach of Glegg and Devenport [15] uses an asymptotic expansion of the roughness height, retaining only the first order term. However, the asymptotic expansion is strictly valid for low frequencies where the hydrodynamic pressure is constant on the roughness elements, and for roughness elements without vertical slope [22]. Despite the limitation of the asymptotic expansion, agreement was found with experiments up to relatively high frequencies [23]. Howe's theory is deemed the most suitable for the particular case under investigation in this paper. In this case there are a relatively low number of large roughness elements with vertical sides. Liu and Dowling's extension of Howe's theory is used, and is summarised in Appendix A.

2.2. Rough wall boundary layer under a favourable pressure gradient

The joint effects of a favourable pressure gradient and roughness on a turbulent boundary layer in the fully rough regime are of interest here. There are a number of studies in the literature focusing on the effect of mild and moderate pressure gradients on the mean and Reynolds stress profiles [24, 25, 26, 27]. Cal *et al.* [24] showed that the effect of roughness on the Reynolds stresses could be scaled with the friction velocity for a zero-pressure gradient and favourable pressure gradient, separately. But no scaling was successful in accounting for roughness and the pressure gradient simultaneously. It was observed that, while roughness increased the ratio of the displacement thickness to the boundary layer thickness (δ^*/δ), a favourable pressure gradient caused it to decrease.

A favourable pressure gradient significantly increased the streamwise Reynolds stresses and skin friction coefficient. On the other side, Coleman *et al.* [28] found that the turbulent kinetic energy decreased in an accelerated rough wall boundary layer, while the shear Reynolds stresses were unaffected by the favourable pressure gradient. They also observed an increase of the roughness Reynolds number along the accelerated rough wall boundary layer, discarding the appearance of transitional effects. Tachie and Shah [25] studied a turbulent channel with two-dimensional roughness. They concluded that the effect of the pressure gradient on the mean and Reynolds stress profiles was much weaker than the effects of roughness, so that the pressure gradient could be ignored. In absence of a pressure gradient, the effect of roughness on the mean and Reynolds stress outer layer profiles has been shown to be accounted for through Townsend's similarity hypothesis, where the equivalent sand grain roughness size with respect to the boundary layer thickness is limited. Castro [19] found a maximum roughness size to boundary layer thickness ratio of approximately 0.4, for the mean velocity profile. Amir and Castro [20] deduced a maximum ratio of 0.2 for the Reynolds stress profiles.

For the point pressure spectrum, several scalings have been proposed that are able to collapse the spectra with and without roughness in the absence of a pressure gradient [29, 30]. In the peak region, the effect of roughness is predicted by the mixed scaling (outer velocity, skin friction and displacement thickness) proposed by Blake [29]. Schloemer [31] observed, for a smooth wall turbulent boundary layer, that a mild favourable pressure gradient caused a sharp decrease of spectral levels at frequencies $f\delta^*/U_o > 0.1$ (where$f$ is the frequency and U_o is the outer velocity). The wavenumber-frequency spectrum of smooth and rough walls peaks at the so-called convective ridge ($2\pi f \approx k_1 U_c, k_3 \approx 0$, where U_c is the eddy convection velocity, and k_1, k_3 are the streamwise and spanwise wavenumbers, respectively). The effect of roughness or a pressure gradient in the vicinity of the convective ridge of the wavenumber-frequency spectrum can be analysed through the changes in eddy convection velocity. Farabee and Geib [8] observed that large roughness caused a decrease in U_c/U_o, which is

equivalent to a shift of the convective ridge to lower frequencies. Schloemer [31] showed that U_c/U_o increased to approximately $0.7 - 0.8$ for a smooth wall turbulent boundary layer in the presence of a mild favourable pressure gradient. Cipolla and Keith [32] observed a sharpening of the convective ridge for increasing favourable pressure gradients. There are a number of models in the literature of pressure wavenumber-frequency spectrum in the absence of pressure gradients. Liu and Dowling [21] showed that they lead to similar roughness noise predictions, and that they are applicable for uniform hemispherical roughness as large as $h/\delta \approx 0.2$ (h is the roughness height, equal to the equivalent sand grain roughness height for this roughness configuration). Alomar *et al.* [4] successfully applied Howe's theory with a scaled smooth wall wavenumber-frequency spectrum to uniform hemispherical roughness of size $h/\delta \approx 0.25$ on average, and $h/\delta \approx 0.5$ for the front row of roughness elements. Furthermore, a weak impact on the roughness noise spectral levels was observed when the ratio h/δ was reduced to less than one in the front row of roughness elements. Even in this extreme situation, with dominant interstitial flow in the leading rows of roughness elements and a ratio $h/\delta > 0.2$ over the entire rough surface, Howe's theory together with the scaled wavenumber-frequency spectrum of Corcos [33] was able to accurately predict the roughness noise spectral levels.

In summary, scalings of the mean flow, Reynolds stresses or the wall pressure spectra that account for roughness and pressure gradients simultaneously are currently not known. This prevents the development of turbulent boundary layer models applicable to arbitrary roughness sizes and pressure gradients. However, well validated models exist for turbulent boundary layers over rough walls in the absence of pressure gradients. These models are applicable *a priori* to equivalent sand grain roughness sizes up to $h_s/\delta \approx 0.2$. However, for the particular case of (hemispherical) roughness noise generation, they have been shown to be applicable to even higher roughness sizes.

Achenbach [34] studied the boundary layers on a rough circular cylinder with roughness sizes up to $h/D = 0.005$ (D is the cylinder diameter). He measured the skin friction distribution along the cylinder surface. The state of

the boundary layer was shown to be a function of the Reynolds number and the roughness size. The higher both the Reynolds number and roughness size were, the further upstream transition occurred, and the further upstream the boundary layer reached a developed state. At a Reynolds number of 3×10^6, transition occurred close to the upstream stagnation line for all roughness sizes.

3. Circular cylinder boundary layer model

The present approach is aimed at high Reynolds number flows typical of aircraft landing gears on approach to landing, i.e. $Re > 10^6$, and the turbulent boundary layer is assumed to be turbulent and fully developed from the upstream stagnation line. The variables that characterise the boundary layer in Howe's theory are the displacement thickness δ^*, wall shear stress τ_w, freestream velocity U_∞, eddy convection velocity U_c, point wall pressure spectrum $\Phi(f)$, and the wall pressure wavenumber-frequency spectrum $\hat{\Phi}(\mathbf{k}, f)$.

Due to the lack of known scalings for the case of rough wall turbulent boundary layers under a favourable pressure gradient, a simple extension of zero-pressure gradient models has been used. It is based on the assumption that the pressure gradient doesn't affect the turbulent boundary layer structure, but only the acceleration of the outer flow. This is accomplished simply by substituting the freestream velocity U_∞ with the outer velocity $U_o(\theta')$ in the equations (the angle θ' is defined in Fig. 1). The resulting boundary layer adapts instantaneously to the change in outer velocity.

Figure 2 shows the outer velocity of the boundary layer along the upstream face of a circular cylinder, obtained in three ways; experimental measurements [34] (with smaller roughness, $h/D = 0.005$), a three-dimensional Delayed Detached-Eddy Simulation (DDES) of a smooth cylinder [35], and a potential flow solution. The trends from the measurements and the simulation are similar up to the separation location. This demonstrates that the outer velocity from the smooth cylinder is a good approximation for the outer velocity of a rough cylinder. The potential flow solution overestimates the outer velocity for

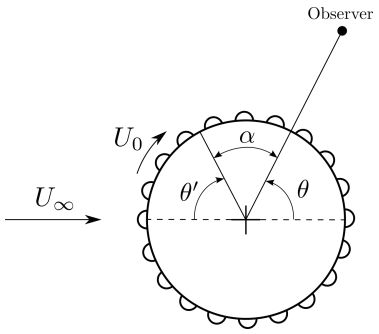

Figure 1: Definition of the polar angles, the freestream velocity U_∞ and the boundary layer outer velocity U_o.

$\theta' > 60°$. The outer velocity obtained from the simulation has been used in the prediction model. Using the smooth bluff body solution increases the simplicity of the prediction model, as only simulations of the smooth bluff body are required.

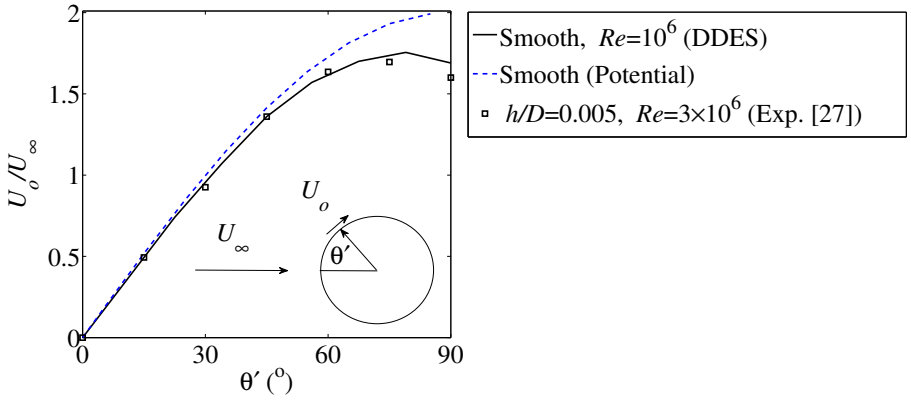

Figure 2: Outer velocity along the boundary layer from a CFD simulation, potential flow solution and experimental data [34].

For a zero-pressure gradient boundary layer, the eddy convection velocity can be approximated as a fraction of the outer velocity, and independent of frequency [36]. It lies within the range $0.5U_\infty < U_c < 0.7U_\infty$. In this proposed

model $U_c(\theta') = 0.65U_o(\theta')$.

The wall shear stress model of Mills and Hang [37] is used, valid in the fully rough regime:

$$c_f(\theta') = \frac{\tau_w}{1/2\rho U_o(\theta')^2} = \left(3.476 + 0.707 \ln\left(\frac{\theta' D}{2h_s}\right)\right)^{-2.46}, \quad (1)$$

where h_s is the equivalent sand grain roughness height. The freestream velocity has been substituted with the outer velocity, which varies along the cylinder surface. The streamwise distance is measured from the upstream stagnation line $x = \theta' D/2$. Figure 3a shows the resulting friction coefficient (denoted by ZPG). Krogstad's model of the mean velocity profile [38] is then used to determine the boundary layer thickness growth:

$$\delta(\theta') = h_s \exp\left(\kappa\sqrt{\frac{2}{c_f(\theta')}} - \kappa B - 2\Pi_o\right) \quad , \quad (2)$$

where $\kappa = 0.41$, $B = 8.5$ and $\Pi_o = 0.45$. In the present case, this law leads to a boundary layer thickness lower than the roughness height for $\theta' < 60°$. In such case the roughness noise model is invalid. Also, the noise levels are overestimated. In order to have a consistent model from the upstream stagnation line, it has been assumed that the boundary layer grows from the top of the roughness. This is accomplished by substituting $\delta(\theta')$ (Eq. 2) for $\delta(\theta') + h_s - \delta(0)$. Figure 3b shows the evolution of the resulting boundary layer thickness. For smaller roughness or longer boundary layers the impact of the region with $\delta < h_s$ with respect to the entire rough region will be lower. Equation. 2 should then be used unmodified. The average roughness height to boundary layer thickness ratio in the range $50° < \theta' < 80°$ (the region with the highest outer velocity) is 0.49. For zero-pressure gradient boundary layers, the displacement thickness can be approximated as a constant fraction of the boundary layer thickness [39], which is also assumed here. The displacement thickness is assumed to be $\delta^*(\theta') = \delta(\theta')/8$. For the densely distributed hemispherical roughness considered in the present study, the equivalent roughness height and the geometrical roughness height are approximately equal.

In addition to this simple estimation of the wall shear stress from a zero-pressure gradient model, the measurements of Achenbach on a rough circular cylinder [34] have been also considered. Even for the largest Reynolds number, where transition happens close to the upstream stagnation line, they show differences with the predictions of Eq. (1). This difference can clearly be seen in Fig. 3a. While Eq. (1) predicts a peak in wall shear stress close to the separation angle, the experimental data shows a peak at approximately $\theta' \approx 55°$. The roughness size in Achenbach's experiments ($h/D = 0.005$) is smaller than the roughness size considered in the present work ($h/D = 0.035$) and the experimental data for skin friction cannot easily be scaled to the roughness size of interest. Therefore, the two different estimations of the wall shear stress corresponding to the rough circular cylinder experimental data (Exp. c_f) and the zero-pressure gradient model (ZPG c_f) will be considered in the prediction model.

The wall pressure spectra corresponding to a zero-pressure gradient boundary layer by Ahn [40] (point spectrum) and Corcos [33] (wavenumber-frequency spectrum) are used (Eq. (A.13) and (A.14), respectively). As explained in section 2.2, the use of these models is theoretically limited to roughness heights $h/\delta < 0.2$, and when the interstitial flow noise sources are negligible. However, previous studies [4, 21] have shown that they still lead to accurate roughness noise predictions for larger hemispherical roughness, even when interstitial flow is dominant in the leading rows of roughness elements.

Finally, the separation location of the boundary layers has to be fixed, as it is assumed that no roughness noise is generated downstream of separation. Detachment occurs further upstream for rough circular cylinders than for smooth circular cylinders [41]. The separation angle (θ'_{sep}) has been estimated indirectly through the shedding Strouhal number, which is directly linked to the wake width. The experimental results of Alomar *et al.* [4] showed a shedding peak Strouhal number for a rough cylinder of 0.19. This value is close to the value that occurs on a smooth cylinder in the sub-critical regime, where separation occurs at approximately 80°. An estimation of the separation angle of 80°

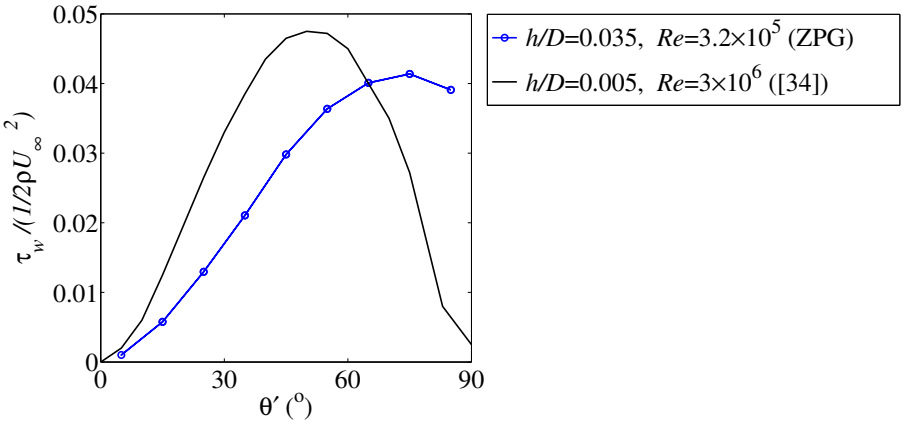

(a)

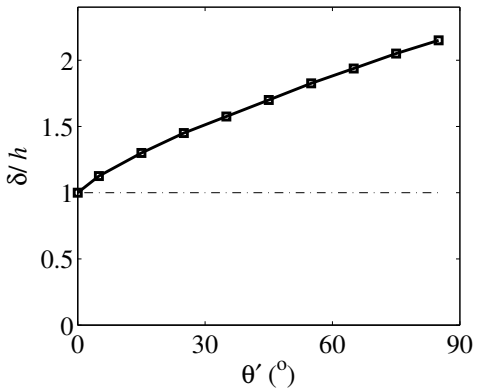

(b)

Figure 3: a) Friction coefficient from the zero-pressure gradient model and experimental data [34], b) boundary layer thickness from the zero-pressure gradient model.

has been used in the prediction model.

In summary, the adapted boundary layer model for the rough circular cylinder is:

- Outer velocity $U_o(\theta')$ estimated from a CFD simulation of a smooth circular cylinder.

- Eddy convection velocity: $U_c(\theta')/U_o(\theta') = 0.65$.
- Skin friction coefficient $c_f(\theta')$ was estimated in two different ways:
  - Zero-pressure gradient model, Eq. (1). Denoted by 'ZPG c_f'.
  - Achenbach's experimental data for a rough circular cylinder. Denoted by 'Exp. c_f'.
- Boundary layer thickness $\delta(\theta') + h_s - \delta(0)$ from zero-pressure gradient boundary layer ($\delta(\theta')$ from Eqs. (1) and (2)).
- Displacement thickness: $\delta^*(\theta')/\delta(\theta') = 1/8$.
- Point pressure spectrum $\Phi(f)$ given by Eq. (A.13).
- Wavenumber-frequency pressure spectrum $\hat{\Phi}(\mathbf{k}, f)$ given by Eq. (A.14).
- Separation angle $\theta'_{\text{sep}} = 80°$.

Two far field noise predictions are calculated, corresponding to the two different estimates of the skin friction coefficient, i.e. the zero-pressure gradient boundary layer model (ZPG c_f) and the experimental data of Achenbach (Exp. c_f) at a smaller roughness height due to the lack of experimental data.

It is important to note that the boundary layer models are applied in a situation where they are likely to be inaccurate. It is argued that the lack of accuracy due to the boundary layer approximations is a reasonable price to pay in order to have a practical prediction model, without the need of prior wind tunnel testing or expensive and time consuming numerical simulations. If experimental or numerical data of any of the boundary layer properties are available, corresponding to the actual rough bluff body, using these data instead of the zero-pressure gradient models should improve the accuracy of the predictions.

4. Boundary Element Method for a circular cylinder

A boundary element method (BEM) is used to account for the scattering of roughness noise by the bluff body. The advantages of BEM over other numerical

techniques for scattering problems are that the Sommerfeld condition at infinity is automatically satisfied, and that there are no dissipation and dispersion errors [42]. In the present case, BEM is used to solve a Helmholtz equation with arbitrary sources, whose solution is a Green's function tailored to the bluff body. Roughness noise theory, adapted to the case of the bluff body, provides the roughness noise source strength distribution. The coupling of the roughness noise sources with the tailored Green's function is described in detail in Section 5. The fast multipole method [42] or similar methods (ACA, etc.) used to speed up BEM have not been implemented since the required computational time was deemed acceptable. The derivation of the BEM algorithm for the present case of a circular cylinder is included in Appendix B.

In the experiments of Alomar *et al.* [4], used to validate the proposed prediction model, the cylinder diameter was $D = 0.127$ m and the freestream velocity was $U_\infty = 40$ m/s. Roughness noise was dominant in the frequency range 2 kHz $< f <$ 6 kHz, with the peak at approximately 3 kHz. The observer distance (r, measured from the cylinder axis) has been limited to $4D$ to reduce the required cylinder spanwise length (L) and keep the ratio r/L small. At that observer distance, the far field scaling $\overline{p^2} \propto 1/r^2$ was verified in the frequency range of interest. The observer is located at the midspan plane of the cylinder, thus the problem is symmetrical with respect to that plane. Using this symmetry, the size of the linear system was reduced by half. The endplates used in the experiments have been ignored.

The following sections describe the setup of the BEM algorithm concerning the shape of the cylinder ends, mesh size and spanwise extent of the cylinder.

4.1. Cylinder ends

Due to the finite cylinder span, the edges and the spanwise extent can have a significant effect. Several geometries of the cylinder ends were considered; hemispherical, flat and empty (no edges). Flat edges cause the linear system to be ill-conditioned. The other two edge treatments provide similar results when the observer distance is small compared with the cylinder length, $r \ll L$. The

comparison between both cases is shown in Fig. 4 for a cylinder of spanwise length 2 m, and a grid with 252 (spanwise)×36 (circumferential) area elements. The differences are small, and for simplicity the geometry with empty edges has been chosen.

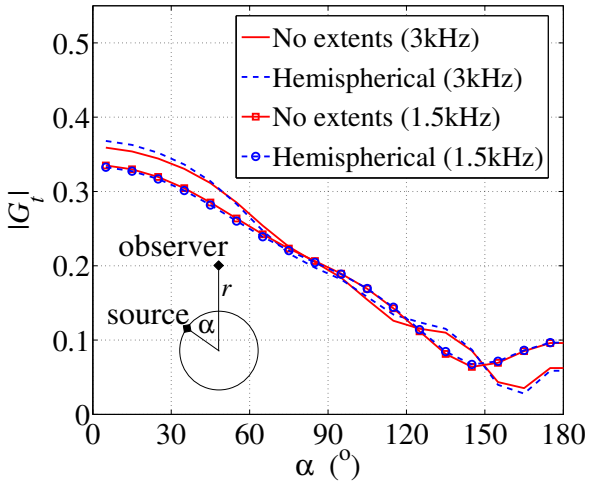

Figure 4: Tailored Green's function $|G_t|$ for the cylinder with hemispherical extents and no extents. On-surface sources are located at an angle α measured from the observer direction, and the observer distance is $4D$.

4.2. Grid size

The two-dimensional case, for which a full analytical Green's function exists [5], has been considered to assess the grid requirements:

$$G_t^{\mathrm{2D}}(\mathbf{x},\mathbf{y},f) = \frac{1}{4\mathrm{j}}\sum_{m=0}^{\infty}\epsilon_m\cos(m\alpha)\big[H_m^1(k_o|\mathbf{x}|)J_m(k_o|\mathbf{y}|) - \\ - \frac{J_{m-1}(k_oD/2)-J_{m+1}(k_oD/2)}{H_{m-1}^1(k_oD/2)-H_{m+1}^1(k_oD/2)}H_m^1(k_o|\mathbf{x}|)H_m^1(k_o|\mathbf{y}|)\big]\,, \quad (3)$$

where $\epsilon_0 = 1$ and $\epsilon_m = 2$ for $m > 0$, k_o is the wavenumber ($= 2\pi f/c$), $\mathbf{x}$ is the observer location, $\mathbf{y}$ is the source location, H_m^1 is the m^{th} order Haenkel function of the first kind, and J_m is the m^{th} order Bessel function.

At 6 kHz, with a cylinder diameter of 0.127 m, 28 grid cells along the circumference of the cylinder gives a resolution of 4 points per wavelength. The spanwise cell size is equal to the circumferential cell size. The grid sensitivity is shown in Fig. 5a, where four grid sizes are compared to the exact solution, at 3 kHz. The medium and fine grids provide accurate results compared to the exact solution, for all relative locations of source and observer. Figure 5b shows the grid sensitivity for the three-dimensional cases. The grid size sensitivity is weak for the two finer meshes. The medium grid, with 36 cells along the circumference, has been used in the roughness noise predictions.

4.3. Cylinder length

The Green's functions corresponding to four different cylinder spanwise lengths are shown in Fig. 6, for a fixed observer distance. The sensitivity to the cylinder length is small. A cylinder of spanwise length (L) of $23.6D$ was used.

5. Coupling of roughness noise with the tailored Green's function

The next step is to couple the roughness noise model to the tailored Green's function obtained from BEM. In the case where the BEM surface mesh is orthogonal and aligned with the boundary layer outer velocity, as is the case for the circular cylinder, the streamwise and spanwise dipole strength distributions (Eqs. (A.11) and (A.12), respectively) can be coupled to the computed tailored Green's functions obtained from BEM in a straightforward manner. First, the acoustic field corresponding to a dipole is directly obtained from two close monopole sources in counterphase. The acoustic field generated by a monopole at $\mathbf{y}_1$ and a monopole at $\mathbf{y}_2$ in counterphase is,

$$p_{\mathrm{dip}}(\mathbf{x}, f) = p_1(\mathbf{x}, f) + p_2(\mathbf{x}, f) = a(f)\big[G_t(\mathbf{x}, \mathbf{y}_1, f) - G_t(\mathbf{x}, \mathbf{y}_2, f)\big] \,. \quad (4)$$

Each roughness element generates a streamwise dipole and a spanwise dipole. The acoustic field is then the sum of a streamwise and a spanwise pair of

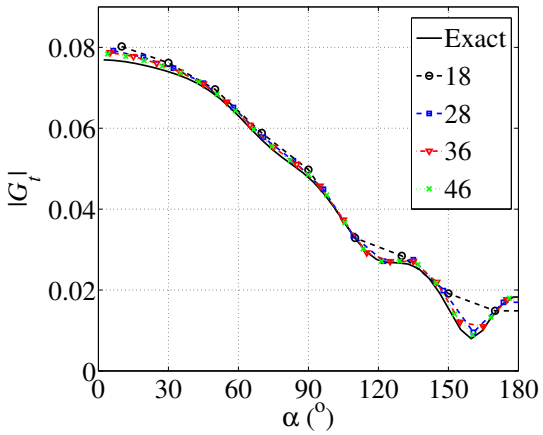

(a)

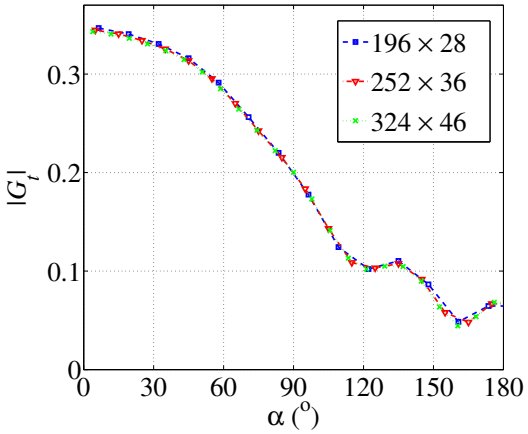

(b)

Figure 5: Tailored Green's function $|G_t|$ at $f = 3$ kHz, for on-surface sources and an observer distance of $4D$ (angle α as defined in Fig. 4). (a) two-dimensional Green's function for various surface mesh sizes (number of azimuthal elements), and (b) three-dimensional tailored Green's function for various surface mesh sizes (spanwise × azimuthal).

monopoles,

$$p_{\text{dip}}(\mathbf{x}, f) = a_{\text{st}}(f)\big[G_t(\mathbf{x}, \mathbf{y}_{\text{st1}}, f) - G_t(\mathbf{x}, \mathbf{y}_{\text{st2}}, f)\big] + a_{\text{sp}}(f)\big[G_t(\mathbf{x}, \mathbf{y}_{\text{sp1}}, f) - G_t(\mathbf{x}, \mathbf{y}_{\text{sp2}}, f)\big] , \quad (5)$$

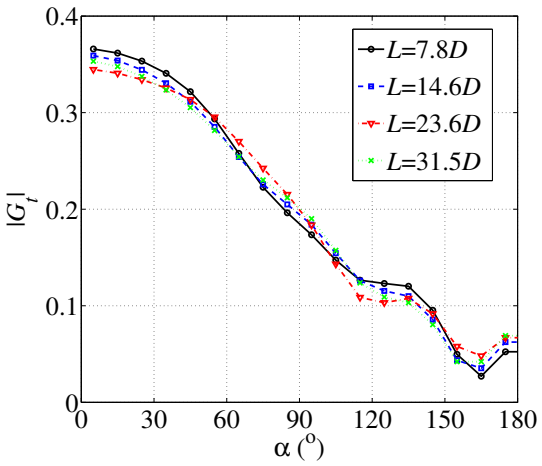

Figure 6: $|G_t|$ for various cylinder lengths and an observer distance of $4D$, with the grid 252 $\times$ 36 elements (angle α as defined in Fig. 4).

where $\mathbf{y}_{\mathrm{st1}}, \mathbf{y}_{\mathrm{st2}}$ are the locations of the monopoles forming the streamwise dipole and $\mathbf{y}_{\mathrm{sp1}}, \mathbf{y}_{\mathrm{sp2}}$ are the locations of the monopoles forming the spanwise dipole. The power spectral density yields,

$$P_{\mathrm{dip}}(\mathbf{x}, f) = \Lambda_{\mathrm{st}}(f) \left| G_t(\mathbf{x}, \mathbf{y}_{\mathrm{st1}}, f) - G_t(\mathbf{x}, \mathbf{y}_{\mathrm{st2}}, f) \right|^2 + \Lambda_{\mathrm{sp}}(f) \left| G_t(\mathbf{x}, \mathbf{y}_{\mathrm{sp1}}, f) - G_t(\mathbf{x}, \mathbf{y}_{\mathrm{sp2}}, f) \right|^2 . \quad (6)$$

The functions $\Lambda_{\mathrm{st}}(f)$ and $\Lambda_{\mathrm{sp}}(f)$ are the streamwise and spanwise dipole strength spectra, respectively (obtained from Eqs. (A.11) and (A.12)). The total acoustic field results from the contribution of all surface elements of area S_i, each containing $N_i = \sigma S_i / \pi h^2$ roughness elements (σ is the roughness surface density, equal to the area covered by roughness elements divided by the total area),

$$P_R(\mathbf{x}, f) = \sum_{i=1}^{N_e} N_i \Lambda_{\mathrm{st},i}(f) \left| G_t(\mathbf{x}, \mathbf{y}_{\mathrm{st1},i}, f) - G_t(\mathbf{x}, \mathbf{y}_{\mathrm{st2},i}) \right|^2 + \sum_{i=1}^{N_e} N_i \Lambda_{\mathrm{sp},i}(f) \left| G_t(\mathbf{x}, \mathbf{y}_{\mathrm{sp1},i}, f) - G_t(\mathbf{x}, \mathbf{y}_{\mathrm{sp2},i}, f) \right|^2 . \quad (7)$$

The height, size and location of the roughness noise dipoles need to be fixed. Liu *et al.* [9] fixed the dipole sources at a distance from the wall equal to

the roughness height. It is known that the accuracy of the Green's function decreases when the sources are at a distance from the surface of the order of the grid size [43]. A two-dimensional case is considered to assess the effect of monopole source height on the acoustic field. Figure 7 shows the Green's function for on-surface sources and off-surface sources at two wall distances, i.e. equal to the roughness height and three times the roughness height. The error of the numerical solution is large when the source height is equal to the roughness height, but is small for the on-surface source. Also the exact solution demonstrates that the acoustic field generated by a monopole in the vicinity of the wall approximates the field generated by a monopole at the wall. Therefore, it is convenient to use the Green's function corresponding to on-surface sources, instead of sources at a small distance from the wall, where the error is large. The calculation of the Green's function for off-surface sources (Eq. (B.1)) is then not necessary.

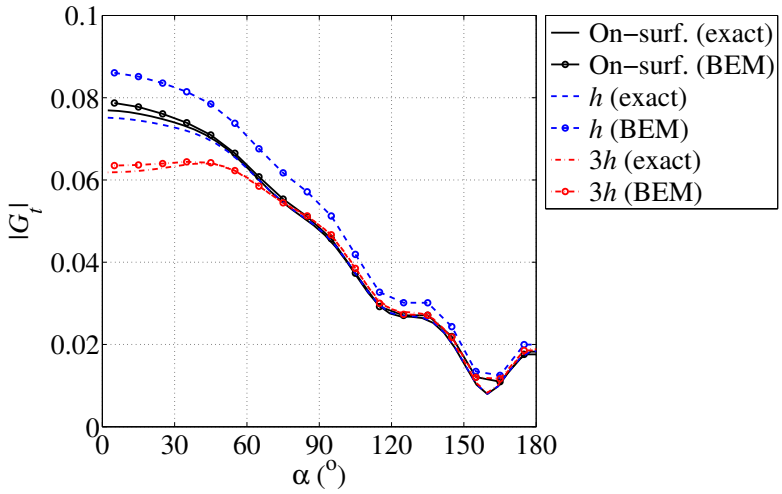

Figure 7: Two-dimensional tailored Green's function $|G_t|$ for on-surface and off-surface sources, with 36 grid elements (angle α as defined in Fig. 4).

The dipole size l_{dip} is not relevant as long as the dipole is acoustically compact ($l_{\text{dip}} \ll \lambda$). In the present configuration where the local outer velocity is

aligned with the surface mesh, the monopole sources at the cell centres can directly be used to form the dipoles as follows. Each cell centre is taken as a dipole centre. Its associated pair of monopoles are fixed at the adjacent cell centres, in the streamwise and spanwise directions. This approach is shown schematically in Fig. 8. This approach results in a dipole size that is two times the grid size. With the grid corresponding to 252×36 surface elements, the dipole size is $l_{\text{dip}} = 2\pi D/36 = 0.2\lambda$, at 3 kHz. Figure 9 shows the field generated by a surface dipole of decreasing size, corresponding to three meshes with decreasing grid size. The difference between the two finest grids is small. A grid size of 252×36 was used in the predictions.

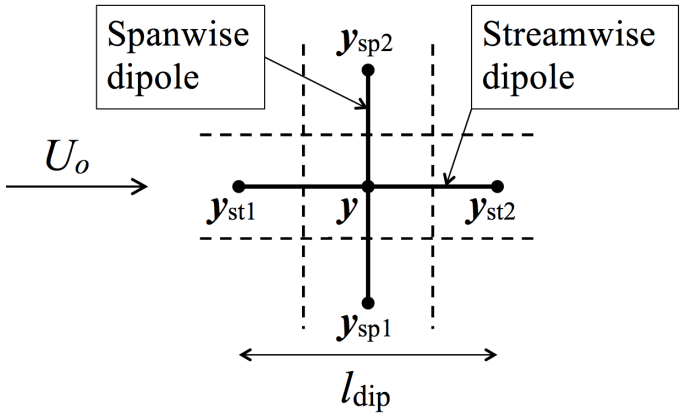

Figure 8: Streamwise and spanwise dipoles centred in $\mathbf{y}$, composed of monopoles located at the adjacent cell centres.

In sections 3, 4 and 5 the boundary layer model and the roughness noise model have been defined for the particular case of a circular cylinder, with the axis perpendicular to the freestream. In such a case, the natural surface mesh is orthogonal and aligned with the boundary layer outer velocity. This mesh is used to compute the boundary layer thickness and friction coefficient, as well as for the BEM. A general methodology, applicable to arbitrary bluff body shapes, is included in Appendix C.

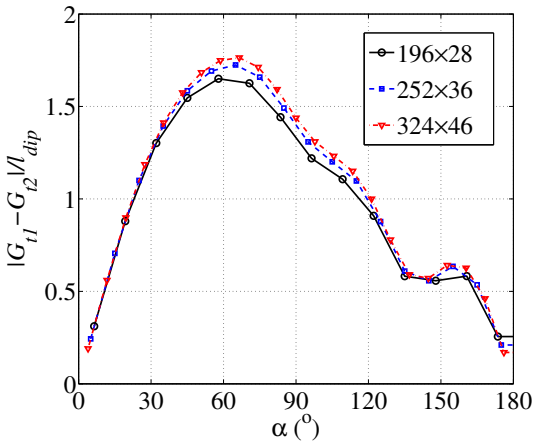

Figure 9: Grid sensitivity of the dipole field $|G_{t1}-G_{t2}|/l_{\mathrm{dip}}$, for observers located at $|\mathbf{x}| = 4D$, at 3 kHz (angle α as defined in Fig. 4).

6. Roughness noise model predictions

6.1. Validation

The roughness configuration used for validation [4] consists of dense hemispherical roughness of height $h/D = 0.035$ and a surface density $\sigma = 0.53$ (area covered by roughness divided by the total area). In addition to the fully covered cylinder, a configuration with roughness elements limited to the usptream face has been considered. Besides roughness noise, surface roughness causes an increase of the broadband bluff body noise levels. This reduces the frequency range where roughness noise is dominant as well as the signal-to-noise ratio (roughness noise levels with respect to the background noise). For this reason, the directivity of the spectral peak level corresponding to the peak roughness noise has been used instead of OASPL. Given there are various relevant lengthscales for roughness noise, the results from the roughness noise model are presented in dimensional frequency.

The predicted spectra at four different observer angles are shown in Fig. 10 using the skin friction coefficient estimated from the zero-pressure gradient

boundary layer model (ZPG c_f) and the experimental data of Achenbach (Exp. c_f). The peak frequency is well predicted for all observation angles. The peak levels are also well predicted at observer angles of $\theta = 83°$ and $\theta = 39°$. However, at observer angles of $\theta = 61°$ and $\theta = 21°$ the levels are under-predicted and over-predicted respectively for both methods of estimating the friction coefficient. The maximum disagreement is approximately 3 dB. Overall, the spectra obtained using both methods of estimating the friction coefficient show similar spectral shapes and levels.

The predicted and measured peak directivity patterns are compared in Fig. 11. The trend is captured reasonably well, although it should be noted that the experimental data had a limited number of observers. There is a local maximum at an observer angle of $\theta = 60°$, with lower levels upstream and downstream of this observer. The skin friction coefficient estimated from Achenbach's experimental data leads to a better agreement with the experimental trend compared to the zero-pressure gradient skin friction model, although the differences are again relatively small.

The predictions discussed above were made with a uniform distribution of surface roughness elements. To test the ability of the prediction method to predict the roughness noise when a bluff body is only partially covered with roughness, a configuration where the roughness is limited to three different angle ranges on the upstream face is tested. The configuration is shown in Fig. 12. The roughness is limited by the angle $\pm\theta'_u$. The measurements for this configuration were performed by Alomar [35], using the same roughness geometry, cylinder size and freestream velocity. Figures 13a and 13b show the measured and predicted spectra at an observer $\theta = 61°$ for various amounts of rough area increasing from upstream: $\theta'_u = \pm 50°, \pm 70°, \pm 180°$. Figures 14a and 14b show the effect of varying the roughness area for an observer at $\theta = 39°$. For the observer at $\theta = 61°$ the reduction of roughness noise between $\theta'_u = 180°$ and $\theta'_u = 70°$ is underpredicted for both skin friction data. The noise reduction between $\theta'_u = 70°$ and $\theta'_u = 50°$ is more accurately predicted, especially for the zero-pressure gradient skin friction model. For the observer at

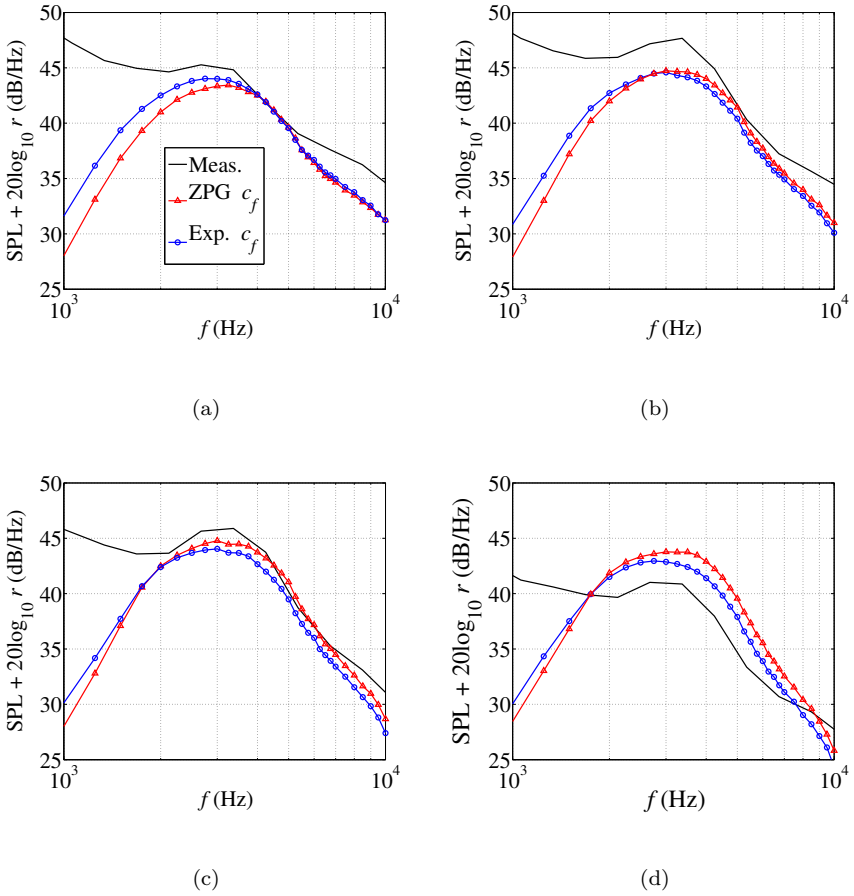

Figure 10: Predicted and measured noise power spectral density, normalised with the observer distance. (a) $\theta = 97°$, (b) $\theta = 61°$, (c) $\theta = 39°$, and (d) $\theta = 21°$.

$\theta = 39°$ the zero-pressure gradient skin friction model predicts the noise levels accurately, while Achenbach's experimental skin friction data leads, again, to underprediction of the noise reduction between $\theta'_u = 180°$ and $\theta'_u = 70°$. For the case where the roughness area is $\theta'_u = \pm 50°$, the roughness noise doesn't appear in the experimental spectra as it is lower than the background and self-noise of the cylinder. Other observer angles show similar trends. Achenbach's skin friction data with smaller roughness size leads to a small difference between the

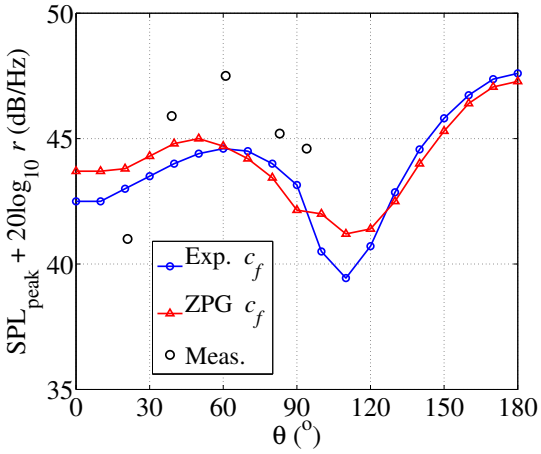

Figure 11: Predicted and measured roughness noise peak levels, normalised with the observer distance, as a function of observer angle.

roughness distribution cases $\theta'_u = 180°$ and $\theta'_u = 70°$ for all observation angles. This can be explained by the low levels of skin friction in the region $\theta' > 70°$. The zero-pressure gradient skin friction model leads to a reasonable prediction of the noise level changes when increasing the area covered by roughness.

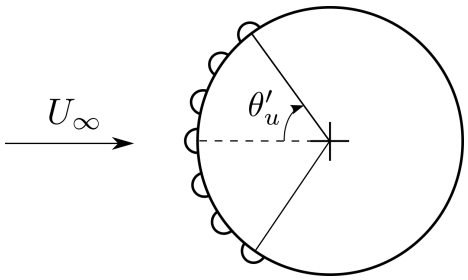

Figure 12: Cylinder partially covered by roughness, with rough area increasing from the upstream stagnation line.

450

The success of the zero-pressure gradient skin friction model is particularly encouraging for industrial applications. For this estimate of skin friction, the adaptation to a bluff body reduces to a simple modification to the outer velocity

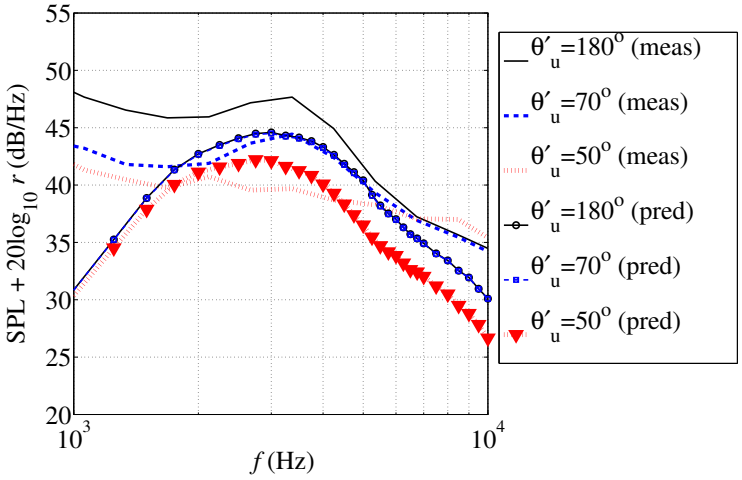

(a)

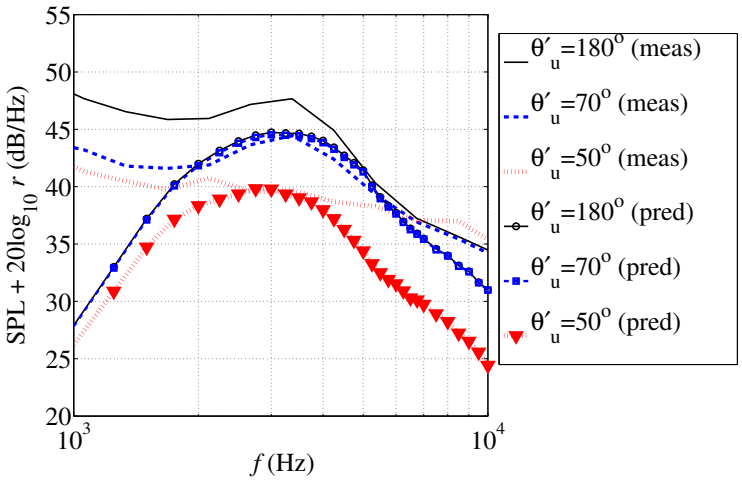

(b)

Figure 13: Predicted and measured spectra at $\theta = 61°$ for the partially covered cylinder with skin friction from: (a) Achenbach's experimental data and (b) from the zero-pressure gradient model.

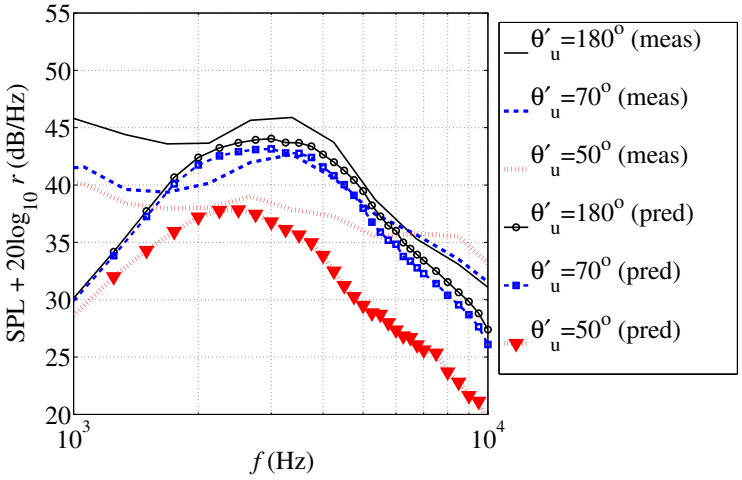

(a)

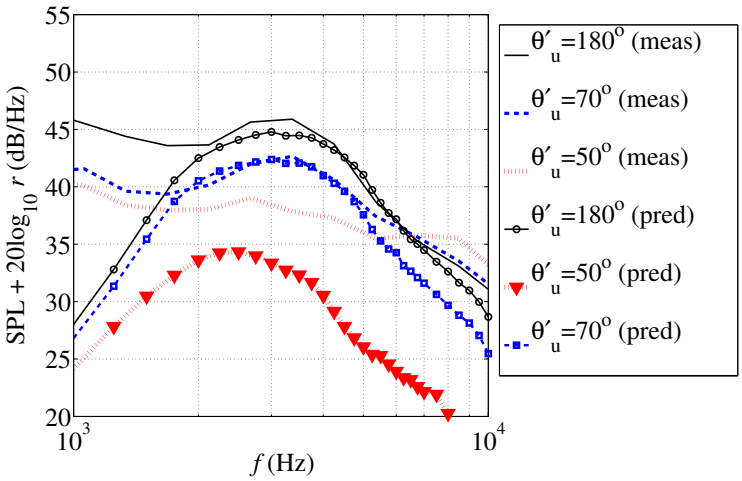

(b)

Figure 14: Predicted and measured spectra at $\theta = 39°$ for the partially covered cylinder with skin friction from: (a) Achenbach's experimental data and (b) from the zero-pressure gradient model.

distribution. The latter can be estimated from a potential flow solution or a CFD simulation of a smooth bluff body.

A simple assessment of the sensitivity of the far field noise levels to changes in the boundary layer properties shows further differences between the two skin friction estimates. Using the zero-pressure gradient skin friction estimate, the predictions show a strong sensitivity to the separation angle and the outer velocity. Conversely, the circular cylinder experimental skin friction estimate has lower sensitivities to these two parameters. This is a consequence of the different distributions of skin friction along the boundary layer. Figure 15 shows the contribution to the far field noise of a roughness noise source located at θ', perceived by an overhead observer. For the zero-pressure gradient skin friction estimate, the sources located further downstream contribute more strongly than for the skin friction estimate from Achenbach's experiments. In general, the accuracy of the prediction model should increase the more information there is available of the boundary layer.

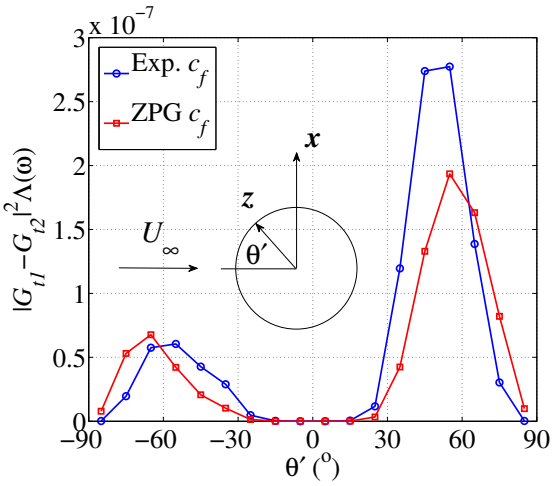

Figure 15: Surface dipole strength weighted with the tailored Green's function at $f = 3$ kHz and at an overhead observer ($\theta = 90°$).

6.2. Effect of roughness surface density and roughness size

The farfield roughness noise is a function of the roughness surface density σ and the roughness size h. Figures 16a and 16b show the effect of varying (σ) on the far field noise directivity and spectrum, respectively, for a given roughness size. The prediction model, with both methods of estimating the skin friction coefficient, shows a weak dependence of the farfield directivity on the roughness density. For the range of roughness surface densities considered, increasing the roughness surface density causes a uniform roughness noise level increase for all observers. Regarding the spectrum, the peak frequency is approximately independent of the roughness surface density, and the offset in magnitude with different surface densities is approximately constant over the frequency range examined.

The directivity plots obtained for three roughness sizes are shown in Fig. 17a, for a given value of roughness surface density. Roughness sizes up to $h/D = 0.063$ have been considered, which corresponds to 13% of the cylinder radius. This value is considered to be small enough that roughness noise generation is not significantly affected by the wall curvature (Howe's theory implies that the wall is locally flat). It is worth addressing the possible effect that an increasing value of h/D may have on the boundary layer. As discussed previously, it is the ratio h/δ which determines the extent to which roughness affects a fully developed turbulent boundary layer. However, a direct effect of increasing h/D can be identified. The attached flow on the cylinder evolves from a laminar boundary layer close to the stagnation line in the vicinity of $\theta' = 0$, to a turbulent boundary layer downstream. It goes through transition and an evolution to a developed state. It seems clear that it is the roughness size that determines the rate of development and growth rate of the attached flow (given a roughness topology and a bluff body Reynolds number). Decreasing the ratio h/D implies a lower number of roughness elements per unit length, and a lower rate of development. Therefore, the boundary layer models based on fully developed flow become less accurate. In such situations, the attached flow would need to be described as flow over obstacles. In the present analysis, the roughness elements

are assumed to be small enough that the attached flow can be approximately described by the turbulent boundary layer models.

The trend of varying roughness size is different for both methods of estimating the skin friction. For the zero-pressure gradient model, an increase in roughness height causes an increase in the roughness noise level at all observers. If the experimental skin friction data is used the trend is more complicated. Observers at $\theta > 60°$ show a decrease in noise level for increasing roughness size, with a small difference between the two smaller sizes. Conversely, observers at $\theta < 60°$ see an increase in levels from $h/D = 0.016$ to $h/D = 0.031$, and a decrease from $h/D = 0.031$ to $h/D = 0.063$. The dependence of the noise spectrum on the roughness height is shown in Fig. 17b, for overhead observers. As expected, increasing roughness sizes shifts the spectral peak to lower frequencies. This is due to the more efficient source scattering of larger eddies, which generate roughness noise at lower frequencies. The peak noise level increases with roughness size for both the zero-pressure gradient friction coefficient model and Achenbach's experimental data, and the peak frequencies are similar. In spite of the differences in the directivity of the overall levels, the effect of increasing roughness size on the spectral features is similar for both friction coefficient versions.

7. Conclusions

A bluff body roughness noise model is proposed and compared to experimental data. The model is an extension of Howe's roughness noise theory to the case of bluff bodies and implicitly assumes that roughness noise generation is analogous to the flat wall case. Conventional BEM is used to account for the scattering of roughness noise by the bluff body, and the roughness noise dipole sources are simulated as pairs of surface monopoles at adjacent grid points. Due to the lack of pressure gradient scalings for rough walls, the effect of pressure gradients has been neglected, and the theory of rough wall turbulent boundary layers has been used. However, it has been adapted to account for the varia-

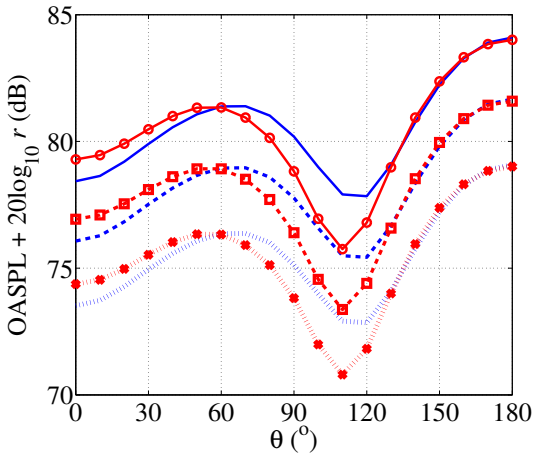

(a)

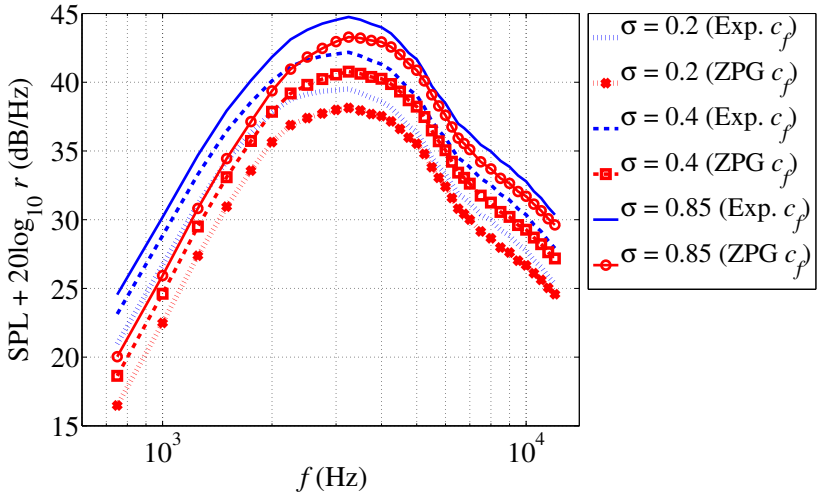

(b)

Figure 16: Dependence of (a) noise directivity and (b) noise spectra at overhead observers on roughness density (σ), for $h/D = 0.031$ and $U_\infty = 40$ m/s.

tion of the boundary layer outer velocity around a bluff body. The model has been implemented and validated for the particular case of a circular cylinder,

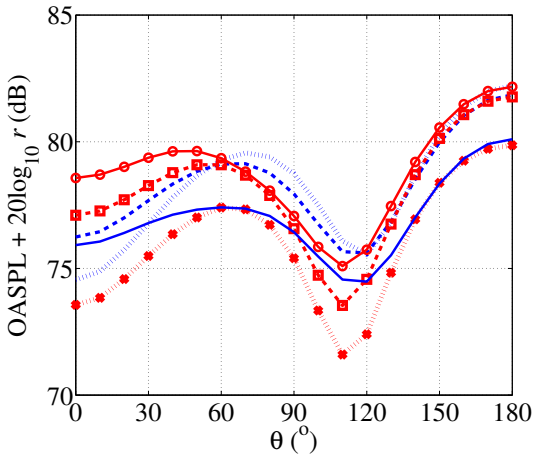

(a)

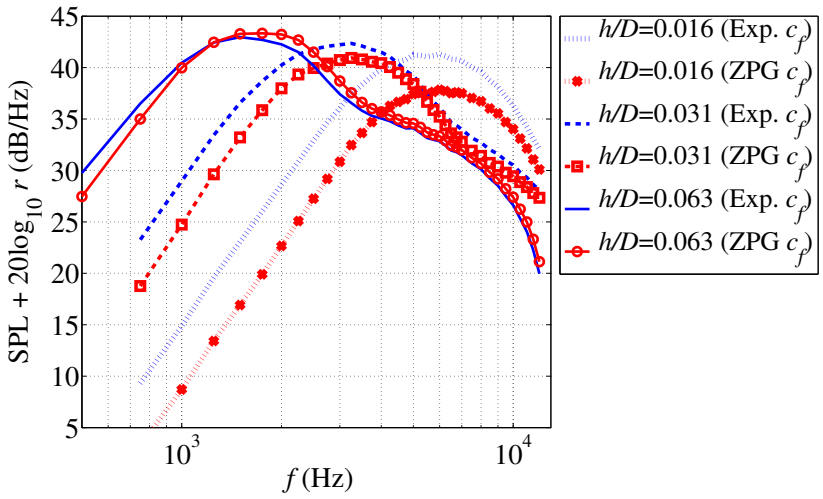

(b)

Figure 17: Dependence of (a) noise directivity and (b) noise spectra at overhead observers on roughness height (h/D) with $\sigma = 0.42$ and $U_\infty = 40$ m/s.

and a general methodology is outlined in Appendix C, applicable to arbitrary geometries. In addition to the simple zero-pressure gradient skin friction model,

experimental data in the literature of the skin friction corresponding to a circular cylinder with smaller roughness has also been considered, leading to different far field noise predictions. The experimental skin friction data corresponds to a significantly smaller roughness size (there is very limited data available of rough wall boundary layers on bluff bodies, or under a favourable pressure gradient). Therefore, it cannot be considered necessarily as correct, or even more accurate than the zero-pressure gradient estimate.

In both approximations of the skin friction, the roughness noise peak frequency is well predicted, and the model captures the experimental trend of the roughness noise peak directivity. The predictions using Achenbach's experimental skin friction coefficient provide a better agreement to the measured roughness noise peak directivity, while the zero-pressure gradient method to estimate the skin friction coefficient leads to a more accurate prediction of the effect of changing the area covered by roughness elements.

A parametric study of the effect of roughness surface density and roughness size has been performed. While for the zero-pressure gradient model of the friction coefficient, the roughness peak noise increases monotonically with roughness size, using the rough circular cylinder skin friction data, results in a more complicated trend at low observer angles. In the considered ranges of roughness surface density and roughness size, the directivity shows a maximum at upstream observers, and local minimas for overhead and downstream observers.

The success of the zero-pressure gradient skin friction model is encouraging. In this case the required knowledge of the boundary layer reduces to the distribution of outer velocity and the separation location, and both can be estimated from a CFD simulation of a smooth bluff body.

Acknowledgements

This research was supported by Airbus.

Appendix A. Roughness noise

Howe's roughness noise model [14], with the extension of Liu and Dowling [9, 21], is summarised. For a small surface element of area S, Liu and Dowling [21] expressed the far field noise spectrum as

$$P_R(\mathbf{x}, f) = \frac{S\sigma\mu_H^2}{4\left|\mathbf{x}\right|^2}\frac{h^4}{\delta^{*4}}\frac{U_c^2}{c^2}\Phi(f)D_f(\psi, \phi, f), \tag{A.1}$$

where δ^* is the displacement thickness, U_c is the eddy convection velocity, and the power spectral density is such that $\overline{p^2} = \int P_R(\mathbf{x}, f)\mathrm{d}f$. μ_H is a roughness density factor introduced by Howe, equal to $1/(1+\sigma/4)$. The function $D_f(\psi, \phi, f)$ contains the directivity information of the emitted sound.

$$D_f(\psi, \phi, f) = Z_1(f)\cos^2\psi + Z_2(f)\sin^2\psi\sin^2\phi \tag{A.2}$$

$$Z_1(f) = \int_0^\infty\int_0^{2\pi}\Gamma\cos^2\eta\mathrm{d}(\left|\mathbf{k}\right|\delta^*)\mathrm{d}\eta, \tag{A.3}$$

$$Z_2(f) = \int_0^\infty\int_0^{2\pi}\Gamma\sin^2\eta\mathrm{d}(\left|\mathbf{k}\right|\delta^*)\mathrm{d}\eta, \tag{A.4}$$

$$\Gamma = \left|\gamma(\left|\mathbf{k}\right|)\right|^2\delta^{*2}\hat{\Phi}(\mathbf{k}, f)\Psi(\left|\mathbf{k}\right|)\exp(-2\left|\mathbf{k}\right|h)(\left|\mathbf{k}\right|\delta^*), \tag{A.5}$$

$$\gamma(\left|\mathbf{k}\right|) = (k_o^2 - \left|\mathbf{k}\right|^2)^{1/2}, \tag{A.6}$$

$$\Psi(\left|\mathbf{k}\right|) = \frac{(1-\sigma J_1(2\left|\mathbf{k}\right|h)/\left|\mathbf{k}\right|h)^3}{1+\sigma J_1(2\left|\mathbf{k}\right|h)/\left|\mathbf{k}\right|h}. \tag{A.7}$$

The radiation direction is defined in terms of the (local) observation angles (ψ, ϕ) defined in Fig. A.1. $J_1(\cdot)$ is the Bessel function of order unity. The $\left|\mathbf{k}\right|\delta^*$-integral upper limit must be specified. The integral upper limit can be taken $\left|\mathbf{k}\right|\delta^* < 25\delta^*/h$ for practical purposes.

The radiated sound by an individual roughness element is comprised of a streamwise dipole and a transverse dipole, corresponding to $Z_1(f)$ and $Z_2(f)$,

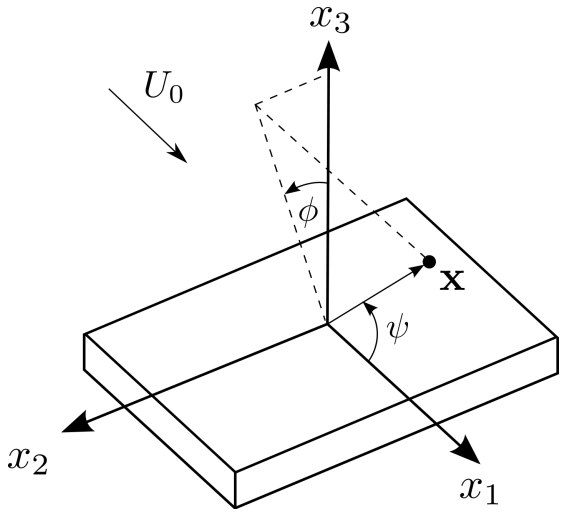

Figure A.1: Definition of the polar angles (ψ, ϕ).

respectively (Eq. (A.2)). The acoustic field radiated by an individual dipole, composed of a pair of monopoles out of phase separated by a distance $l_{\rm dip}$ is

$$\begin{aligned} p_{\rm dip}(\mathbf{x}, f) &= p_1(\mathbf{x}, f) + p_2(\mathbf{x}, f) = \frac{a(f)}{4\pi|\mathbf{x}_1|} e^{ik_o|\mathbf{x}_1|} - \frac{a(f)}{4\pi|\mathbf{x}_2|} e^{ik_o|\mathbf{x}_2|} \\ &\approx \frac{a(f)}{4\pi|\mathbf{x}|} e^{ik_o|\mathbf{x}|} ik_o l_{\rm dip} \cos\psi. \end{aligned} \tag{A.8}$$

The calculation of the power spectral density is straightforward, since the function multiplying the source strength is deterministic,

$$P_{\rm dip}(\mathbf{x}, f) = \Lambda(f) \left| \frac{ik_o l_{\rm dip} \cos\psi}{2\pi|\mathbf{x}|} e^{ik_o|\mathbf{x}|} \right|^2 = \frac{\Lambda(f) k_o^2 l_{\rm dip}^2}{4\pi^2|\mathbf{x}|^2} \cos^2\psi, \tag{A.9}$$

where $\Lambda(f)$ is the power spectral density of the source strength. This expression, with the contribution from N dipoles, must equal the far field roughness noise of Eq. (A.1), which determines the streamwise dipole strength,

$$\frac{N\Lambda_{\rm st}(f) k_o^2 l_{\rm dip}^2}{4\pi^2|\mathbf{x}|^2} \cos^2\psi = \frac{S\sigma\mu_H^2}{4\,|\mathbf{x}|^2} \frac{h^4}{\delta^{*4}} \frac{U_c^2}{c^2} \Phi(f) Z_1(f) \cos^2\psi, \tag{A.10}$$

$$\Lambda_{\rm st}(f) = \frac{\pi\mu_H^2}{4} \left(\frac{h}{l_{\rm dip}}\right)^2 \left(\frac{h}{\delta^*}\right)^4 \left(\frac{U_c}{f}\right)^2 \Phi(f) Z_1(f). \tag{A.11}$$

The relation $\sigma = N\pi h^2/S$ has been used. If the same is done for the spanwise dipoles it yields

$$\Lambda_{\mathrm{sp}}(f) = \frac{\pi \mu_H^2}{4} \left(\frac{h}{l_{\mathrm{dip}}}\right)^2 \left(\frac{h}{\delta^*}\right)^4 \left(\frac{U_c}{f}\right)^2 \Phi(f) Z_2(f). \tag{A.12}$$

The wall pressure point spectrum by Ahn [40] is

$$\Phi(f) = \left(\frac{\tau_w \delta^*}{U_o}\right) \frac{16.56\pi Sh^{*0.8}}{1 + 4.1 Sh^{*1.7} + 4.4 \times 10^{-4} Sh^{*5.9}}, \tag{A.13}$$

where $Sh^* = 2\pi f \delta^*/U_o$. The wall pressure wavenumber-frequency spectrum by Corcos [33] is

$$\hat{\Phi}(\mathbf{k}, f) = \frac{(2\pi f)^2}{U_c^2} \frac{4\alpha_1 \alpha_3}{(\alpha_1^2 + (U_c \kappa_1/(2\pi f) - 1)^2)(\alpha_3^2 + U_c^2 \kappa_3^2/(2\pi f)^2)}, \tag{A.14}$$

where $\alpha_1 = 0.1$ and $\alpha_3 = 0.77$.

The inputs of the roughness noise model are the eddy convection velocity, the boundary layer outer velocity, the boundary layer displacement thickness and the skin friction.

Appendix B. BEM algorithm for a circular cylinder

From Green's identities and Helmholtz's equation with wall boundary conditions, a boundary integral equation for the Green's function tailored to the body surface is obtained [44],

$$G_t(\mathbf{x}, \mathbf{y}, f) = G_o(\mathbf{x}, \mathbf{y}, f) + \iint_\Sigma G_t(\mathbf{x}, \mathbf{z}, f) \frac{\partial G_o(\mathbf{z}, \mathbf{y}, f)}{\partial z_i} n_i \mathrm{d}^2\mathbf{z}, \tag{B.1}$$

for off-surface sources located in $\mathbf{y}$ and on-surface sources in $\mathbf{z}$. When the off-surface sources are brought arbitrarily close to a surface mesh point $\mathbf{z}_p$, the equation becomes

$$G_t(\mathbf{x}, \mathbf{z}_p, f) \left(1 - \frac{\Omega(\mathbf{z}_p)}{4\pi}\right) = G_o(\mathbf{x}, \mathbf{z}_p, f) + \iint_\Sigma G_t(\mathbf{x}, \mathbf{z}, f) \frac{\partial G_o(\mathbf{z}, \mathbf{z}_p, f)}{\partial z_i} n_i \mathrm{d}^2\mathbf{z}. \tag{B.2}$$

$\Omega(\mathbf{z}_p)$ is the solid angle, which is equal to 2π for a (locally) smooth surface. This is a boundary integral equation whose only unknown is $G_t(\mathbf{x}, \mathbf{z}_p, f)$, and has to be solved numerically. The conventional BEM used in the present work,

consists of solving this equation using a surface discretization of the boundary integral equation, to convert the above equation into a linear system of equations, with as many equations as surface elements. A piece-wise representation of the Green's function is used on the surface, the surface integration being of second order. The solution corresponds to the particular values taken for the observer location $\mathbf{x}$ and frequency f, i.e. for every pair $(\mathbf{x}, f)$ the linear system must be solved.

$$G_t(\mathbf{x}, \mathbf{z}_{pi}, f)\left(1 - \frac{\Omega(\mathbf{z}_{pi})}{4\pi}\right) = G_o(\mathbf{x}, \mathbf{z}_{pi}, f) + \sum_{j=1, j\neq i}^{N_e} G_t(\mathbf{x}, \mathbf{z}_j, f)\frac{\partial G_o(\mathbf{z}_j, \mathbf{z}_{pi}, f)}{\partial z_n}\Delta S(\mathbf{z}_j), \text{ for } i = 1, ..., N_e, \tag{B.3}$$

where z_n is the wall normal coordinate. For a circular cylinder the free field Green's function and its wall normal derivatives are

$$G_o(\mathbf{x}, \mathbf{z}_{pi}, f) = \frac{e^{ik_o|\mathbf{x}-\mathbf{z}_{pi}|}}{4\pi\,|\mathbf{x} - \mathbf{z}_{pi}|}, \tag{B.4}$$

$$\frac{\partial G_o(\mathbf{z}_j, \mathbf{z}_{pi}, f)}{\partial z_n} = \frac{e^{ik_o|\mathbf{z}_j-\mathbf{z}_{pi}|}}{4\pi\,|\mathbf{z}_j - \mathbf{z}_{pi}|^3}\left(ik_o\,|\mathbf{z}_j - \mathbf{z}_{pi}| - 1\right)(\mathbf{z}_j - \mathbf{z}_{pi}) \cdot \mathbf{n}_j. \tag{B.5}$$

Note that the free-field Green's function diverges when $\mathbf{z}_j \to \mathbf{z}_{pi}$, but the integral exists. In the numerical integration the surface element corresponding to $\mathbf{z}_{pi}$ is excluded, eliminating the divergence. If the surface elements are small enough the contribution to the integral of that surface element is negligible. The matrix coefficients of the linear system are:

$$A_{ij} = \begin{cases} \Delta S(\mathbf{z}_j)\frac{\partial G_o(\mathbf{z}_j, \mathbf{z}_{pi}, f)}{\partial z_n}, & \text{if } i \neq j. \\ -1/2, & \text{if } i = j. \end{cases} \tag{B.6}$$

Finally, the following linear system needs to be solved:

$$A_{ij}G_t(\mathbf{x}, \mathbf{z}_{pi}, f) = G_o(\mathbf{x}, \mathbf{z}_{pi}, f). \tag{B.7}$$

The matrix of the resulting linear system is full and non-symmetric in general. The number of operations to solve the system using one of the conventional methods (LU decomposition, Gauss elimination) is proportional to N_e^3. In the present case LU decomposition with partial pivoting has been used. The surface mesh is parameterised using cylindrical coordinates, with uniform spacing.

Appendix C. Methodology for arbitrary bluff body shapes

We outline in the following a general methodology for the roughness noise prediction model, which is applicable to arbitrary bluff body shapes. It consists of the following steps:

1. Perform a CFD simulation of the smooth bluff body. The boundary layer outer velocity U_o obtained is directly used for the case with roughness. The eddy convection velocity is estimated from the zero-pressure gradient model: $U_c = 0.65U_o$. If a viscous solver is used, the resulting flow field provides an estimation of the separation angle. If a potential solver is used, the separation angle must be estimated by other means.
2. Define a (structured) orthogonal surface mesh on the bluff body aligned with the boundary layer outer velocity.
3. The skin friction coefficient c_f and the boundary layer thickness δ are computed from the zero-pressure gradient models (Eqs. (1) and (2), respectively), along the streamlines defined by the surface mesh. In the case that the boundary layer thickness is lower than the roughness height in a significant portion of the boundary layer, the boundary layer thickness growth can be computed from the top of the roughness. The boundary layer displacement thickness is taken as $\delta^* = \delta/8$. For a general bluff body shape, the angle θ' used for the circular cylinder case would be a position coordinate running along a streamline defining the surface mesh. The point pressure spectrum $\Phi(f)$ and the wavenumber-frequency pressure spectrum $\hat{\Phi}(\mathbf{k}, f)$ on the body surface are computed from Eqs. (A.13)

and (A.14), respectively. If available, experimental values of any of these variables can be used instead of the zero-pressure gradient models.

4. If possible, BEM is computed using the orthogonal surface mesh defined in step 2. If this is not possible, the BEM should be computed on any other desired mesh. The result is the tailored Green's function G_t with the monopole sources located at the surface cell centres.

5. If the BEM surface mesh used is orthogonal and aligned with the boundary layer outer velocity, the streamwise dipole strength spectrum $\Lambda_{\mathrm{st}}(f)$ and the spanwise dipole strength spectrum $\Lambda_{\mathrm{sp}}(f)$ corresponding to each cell centre within the attached flow region are computed from Eqs. (A.11) and (A.12), respectively (see Fig. 8). If the BEM mesh is not orthogonal and/or not aligned with the boundary layer outer velocity, the Green's function corresponding to on-surface sources located on a mesh orthogonal and aligned with the boundary layer outer velocity is determined from interpolation. The streamwise and spanwise dipole strengths can then be determined from Eqs. (A.11) and (A.12), respectively.

6. The far field noise spectrum $P_R(\mathbf{x}, f)$ is computed from Eq. (7).

References

[1] M. R. Fink, Noise component method for airframe noise, Journal of Aircraft 16 (10) (1979) 801–820.

[2] Y. Guo, A statistical model for landing gear noise prediction, Journal of Sound and Vibration 282 (1) (2005) 61–87.

[3] Y. Guo, Empirical prediction of aircraft landing gear noise, Tech. Rep. NASA/CR-2005-213780, NASA (2005).

[4] A. Alomar, D. Angland, X. Zhang, Experimental study of noise emitted by circular cylinders with large roughness, Journal of Sound and Vibration 333 (24) (2014) 6474–6497.

[5] X. Gloerfelt, F. Perot, C. Bailly, D. Juve, Flow-induced cylinder noise formulated as a diffraction problem for low mach numbers, Journal of Sound and Vibration 287 (1) (2005) 129–151.

[6] A. H. W. M. Kuijpers, G. Verbeek, J. W. Verheij, An improved acoustic fourier boundary element method formulation using fast fourier transform integration, Journal of the Acoustical Society of America 102 (3) (1997) 1394–1401.

[7] A. S. Hersh, Experimental investigation of surface roughness generated flow noise, no. 1983-0786, 8th AIAA Aeroacoustics Conference, AIAA, Atlanta, Georgia, 1983.

[8] T. M. Farabee, F. E. Geib, Measurements of boundary layer pressure fluctuations at low mach numbers on smooth and rough walls, ASME Symposium on Flow Noise Modelling, Measurement and Control 11 (1991) 55–68.

[9] Y. Liu, A. P. Dowling, H.-C. Shin, Measurement and simulation of surface roughness noise using phased microphone arrays, Journal of Sound and Vibration 314 (1) (2008) 95–112.

[10] W. Devenport, D. L. Grissom, W. N. Alexander, B. S. Smith, S. A. L. Glegg, Measurements of roughness noise, Journal of Sound and Vibration 330 (17) (2011) 4250–4273.

[11] W. N. Alexander, W. Devenport, S. A. L. Glegg, Aerodynamic noise from sparse surface roughness, no. 2011-2740, 17th AIAA/CEAS Aeroacoustics Conference, AIAA, Portland, Oregon, 2011.

[12] Q. Yang, M. Wang, Computational study of roughness-induced boundary-layer noise, AIAA Journal 47 (10) (2009) 2417–2429.

[13] Q. Yang, M. Wang, Boundary-layer noise induced by arrays of roughness elements, Journal of Fluid Mechanics 727 (2013) 282–317.

[14] M. S. Howe, On the generation of sound by turbulent boundary layer flow over a rough wall, Proceedings of the Royal Society A 395 (1809) (1984) 247–263.

[15] S. A. L. Glegg, W. Devenport, The far-field sound from rough-wall boundary layers, Proceedings of the Royal Society A 465 (2009) 1717–1734.

[16] A. V. Smol'yakov, Noise of a turbulent boundary layer flow over smooth and rough plates at low mach numbers, Acoustical Physics 47 (2) (2001) 218–225.

[17] A. A. Townsend, The structure of turbulent shear flow, Cambridge University Press, Cambridge, 1976.

[18] K. A. Flack, M. P. Schultz, T. A. Shapiro, Experimental support for townsend's reynolds number similarity hypothesis on rough walls, Physics of Fluids 17 (3) (2005) 1–9.

[19] I. Castro, Rough-wall boundary layers: mean flow universality, Journal of Fluid Mechanics 585 (2007) 469–485.

[20] M. Amir, I. P. Castro, Turbulence in rough wall boundary layers: universality issues, Experiments in Fluids 51 (2) (2011) 313–326.

[21] Y. Liu, A. P. Dowling, Assessment of the contribution of surface roughness to airframe noise, AIAA Journal 45 (4) (2007) 855–869.

[22] M. S. Howe, The turbulent boundary layer rough-wall pressure spectrum at acoustic and subconvective wavenumbers, Proceedings of the Royal Society A 415 (1848) (1988) 141–161.

[23] W. N. Alexander, W. Devenport, S. A. L. Glegg, Predictive limits of acoustic diffraction theory for rough wall flows, AIAA Journal 52 (3) (2014) 634–642.

[24] R. B. Cal, B. Brzek, T. G. Johansson, L. Castillo, The rough favourable pressure gradient turbulent boundary layer, Journal of Fluid Mechanics 641 (2009) 129–155.

[25] M. F. Tachie, M. K. Shah, Favorable pressure gradient turbulent flow over straight and inclined ribs on both channel walls, Physics of Fluids 20 (9) (2008) 1–22.

[26] G. F. K. Tay, D. C. S. Kuhn, M. F. Tachie, Particle image velocimetry study of rough-wall turbulent flows in favorable pressure gradient, Journal of Fluids Engineering 131 (6) (2009) 1–12.

[27] J. H. Shin, S. J. Song, Pressure gradient effects on smooth and rough surface turbulent boundary layerspart i: favorable pressure gradient, Journal of Fluids Engineering 137 (1) (2015) 1–9.

[28] H. W. Coleman, R. J. Moffat, W. M. Kays, The accelerated fully rough turbulent boundary layer, Journal of Fluid Mechanics 82 (1977) 507–528.

[29] W. K. Blake, Turbulent boundary-layer wall-pressure fluctuations on smooth and rough walls, Journal of Fluid Mechanics 44 (1970) 637–660.

[30] T. Meyers, J. B. Forest, W. J. Devenport, The wall-pressure spectrum of high-reynolds-number turbulent boundary-layer flows over rough surfaces, Journal of Fluid Mechanics 768 (2015) 261–293.

[31] H. H. Schloemer, Effect of pressure gradients on turbulent boundary layer wall pressure fluctuations, Journal of the Acoustical Society of America 42 (1) (1967) 93–113.

[32] K. Cipolla, W. Keith, Effects of pressure gradients on turbulent boundary layer wave number frequency spectrum, AIAA Journal 38 (10) (2000) 1832–1836.

[33] G. M. Corcos, The structure of the turbulent pressure field in boundary-layer flows, Journal of Fluid Mechanics 18 (1978) 353–378.

[34] E. Achenbach, Influence of surface roughness on the cross-flow around a circular cylinder, Journal of Fluid Mechanics 46 (1971) 321–335.

[35] A. Alomar, Investigation into noise emitted by bluff bodies with large roughness, Ph.D. thesis, Faculty of Engineering and the Environment, University of Southampton, Southampton (2013).

[36] D. M. Chase, Modelling the wavevector-frequency spectrum of turbulent boundary layer wall pressure, Journal of Sound and Vibration 70 (1) (1980) 29–67.

[37] A. F. Mills, X. Hang, On the skin friction coefficient for a fully rough flat plate, Journal of Fluids Engineering 105 (3) (1983) 364–365.

[38] P. A. Krogstad, R. A. Antonia, L. W. B. Browne, Comparison between rough- and smooth-wall turbulent boundary layers, Journal of Fluid Mechanics 245 (1992) 599–617.

[39] M. S. Howe, Acoustics of fluid-structure interactions, Cambridge University Press, Cambridge, 1998.

[40] B. Ahn, Modelling unsteady wall pressures beneath turbulent boundary layers, Ph.D. thesis, Department of Engineering, University of Cambridge, Cambridge (2005).

[41] O. Guven, C. Farell, V. C. Patel, Surface roughness effects on the mean flow past circular cylinders, Journal of Fluid Mechanics 98 (1980) 673–701.

[42] G. D. Manolis, D. Polyzos, Recent advances in boundary element methods, Springer, 2009.

[43] Y. Khalighi, D. Bodony, Improved near-wall accuracy for solutions of the helmholtz equation using the boundary element method, Tech. rep., Center for Turbulence Research, Stanford University (2006).

[44] T. Takaishi, M. Miyazawa, C. Kato, A computational method of evaluating noncompact sound based on vortex sound theory, Journal of the Acoustical Society of America 121 (3) (2007) 1353–1361.